Article

Optimal Design of PV Inverter Using LCOE Index †

Morteza Tadbiri-Nooshabadi [1,2,*]**, Jean-Luc Schanen** [2,*] **, Shahrokh Farhangi** [1]**, Hossein Iman-Eini** [1]
and Corentin Rizet [3]

1 School of Electrical and Computer Engineering, College of Engineering, University of Tehran,
Tehran 14399-57131, Iran
2 Grenoble INP, G2Elab, Univ. Grenoble Alpes, CNRS, 38000 Grenoble, France
3 SIREPE, 540 Route de la Tour, 73460 Montailleur, France
* Correspondence: m.tadbiri@ut.ac.ir (M.T.-N.); jean-luc.schanen@grenoble-inp.fr (J.-L.S.)
† This paper is an extended version of our paper published in 2022 24th European Conference on Power
Electronics and Applications (EPE'22 ECCE Europe), Hannover, Germany, 5–9 September 2022.

Abstract: This work uses design optimization of a power electronics converter to achieve the best levelized cost of energy in a PV application. The methodology uses detailed models of power electronics' active and passive components to determine the cost and performances of the solid-state energy conversion and connect them to the system-level vision. The deterministic algorithm used for converter sizing allows taking into account a large number of variables and constraints. Methodology, models, and some illustrations of the results are provided in this paper. A sensitivity analysis was also conducted on the cost model.

Keywords: design optimization; photovoltaic; levelized cost of energy; reliability; cost analysis

1. Introduction

Photovoltaic (PV) technology requires a high-efficiency power conversion in order to achieve an acceptable price per produced kWh. Indeed, the cost of power converters is not negligible in the installation and usually accounts for about 6 to 9 percent of overall installation costs depending on the type of installation (utility scale, commercial scale, and residential scale) [1]. Both the cost and performance of the power electronics conversion depend on the choice of components and the converter sizing: for instance, silicon carbide metal–oxide semiconductor field-effect transistors (SiC-MOSFET) are more expensive than silicon insulated-gate bipolar transistors (Si-IGBT) but exhibit lower losses. The choice is therefore not straightforward. On the other hand, it is well known that the efficiency of a power converter depends on its nominal power [2] as well as its cost. Therefore, the design of a converter and the associated components ratings becomes a crucial issue.

In order to quantify and compare the cost of different energy technologies, the levelized cost of energy (LCOE) index is generally used [3]. LCOE represents the price at which the electricity is generated from a specific energy source over the whole lifetime of the generation unit. The index is expressed by:

$$LCOE = \frac{Total\ life-cycle\ cost}{Total\ lifetime\ energy\ production} \qquad (1)$$

Based on the above expression, a cost-effective grid-connected PV system can be obtained by minimizing the initial investment cost which is included the cost of the PV system components (e.g., PV modules, DC/AC inverters, etc.), maximizing the amount of energy injected into the grid and increasing its reliability. The lifetime of the PV system components is indeed very important since any failure in operational time causes missing PV energy [4]. The injected energy into the grid is upped by a maximum power point tracker (MPPT) control algorithm [5].

The rule of thumb for solar inverter overclocking is that solar panel capacity should not be more than roughly 30% greater than inverter capacity. More scientific work has already been conducted on the optimal sizing of PV inverters, using various models and algorithms [6]. From the modeling point of view, a database of existing inverters, simulations, or simple analytical models has been reported [6,7]. Obviously, the mission profile is always taken into account in these kinds of studies. This mission profile lists irradiation and temperature for each day of the year [8].

However, converter-level analytical models are only representative of global behavior and cannot reflect precisely the impact of technological choice and component design. A database of existing hardware is by definition limited to available technologies and cannot be used to investigate potential breakthroughs or unconventional designs. Precise simulation of the power electronics converter can of course be used to obtain the performances depending on the technological choices and inverter design, but it is very long and not really compatible with optimization, especially if various technological or structural options are considered.

Therefore, this paper proposes a methodology that is clearly optimization-oriented, based on component models to obtain the minimum levelized cost of energy (LCOE) of the power electronics part only. When dealing with cost evaluation, it is important to note that an electronic system design is not solely influenced by component prices. There are also significant costs associated with tests and validations (functional, control, and also certification, including safety, electromagnetic compatibility (EMC), etc.). Figure 1 shows how each part of the manufacturing process contributes to the process. These data are extracted from the authors' expertise in design and fabrication in France. Obviously, other regions in the world may have different numbers. From this figure, it is estimated that the cost of components makes up almost 60 percent of the total cost of the converter, whereas the cost of other components such as testing, mechanical, and assembling makes up almost 40 percent.
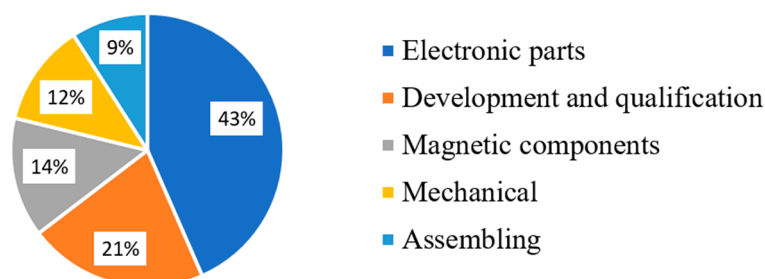
Figure 1. The contribution of each part of the manufacturing process for a 15 kW PV inverter and French manufacturer.

This paper discusses comparisons between various technological choices, such as the sizing power of the converter, which does not significantly modify the cost of tests and validation. The purpose of this paper is to examine how converter design can affect LCOE, not how a company can save costs in other areas. For this reason, it is assumed that the cost of all items not related to the converter design is constant. Therefore, the inverter cost will be evaluated based on the component cost only; the rest of the cost will be kept constant.

Each part of the PV inverter and MPPT boost converter is considered and the global performances of the conversion take into account component behavior and sizing. Several constraints are addressed in the optimization: device-level constraints (such as the semiconductor maximum temperature), as well as system-level constraints (such as THD on the AC side). Section 2 will illustrate the interest in having a precise representation of the converter's performances based on a case study using three different manufacturers. Section 3 will then provide all models used in the converter's optimization, as well as the optimization methodology, which is based on a deterministic algorithm. The lifetime

prediction is also evaluated in this section. Section 4 will present some optimization results for various cases.

2. LCOE of Industrial Inverters: Case Study

The evaluation of the performances of a PV inverter has to be achieved with respect to the balance between the investment cost (the price of the inverter if we focus on this part of the PV system only) and the amount of energy produced in the product's lifetime. In order to quantify and compare the cost for different situations, the levelized cost of energy (LCOE) index will be used for the converters. For this purpose, the mission profile of the PV inverter has first to be defined, and the efficiency of the inverter vs. power to be considered. Figure 2 shows three case studies of the same power (20 kVA) provided in manufacturer datasheets [9–11]. To enlarge this study, two different locations were considered (Grenoble, France and Tehran, Iran), with different irradiation characteristics.
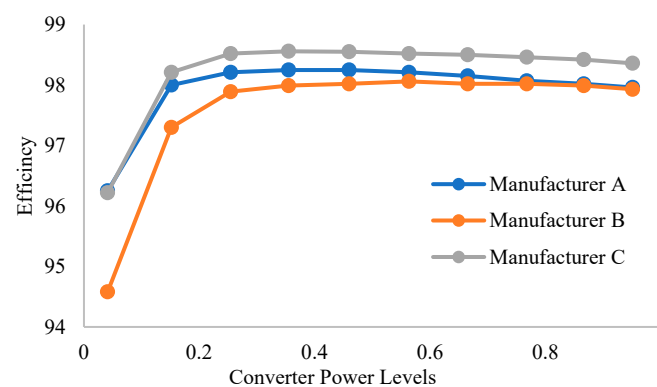

Figure 2. The inverter efficiency curve for three different 20 kVA inverters.

The mission profile was developed based on local measurements. Data points were taken every 10 min, corresponding to the 10-min average of irradiance and ambient temperature. The mean daily profiles, averaged over the duration of the considered data in Grenoble, are shown in Figure 3. It was then split into 10 steps for operational phases and one step for dormant phase (Figure 4); for example, an application that is a 20 kW installation, composed of 4 strings of 16 * 320 W panels (Figure 5). By using the method of [12], Table 1 shows the mission profile data at Grenoble and Tehran in each step.
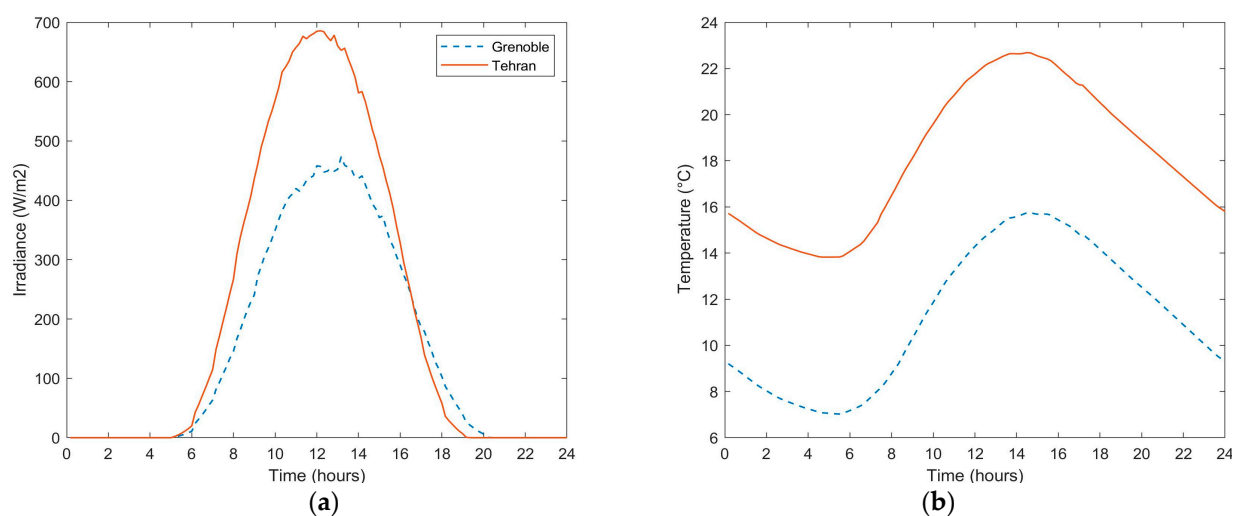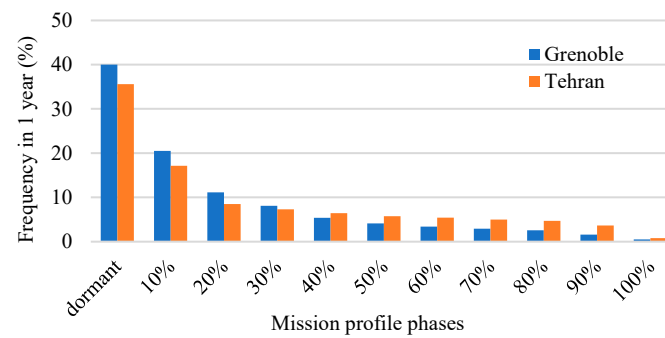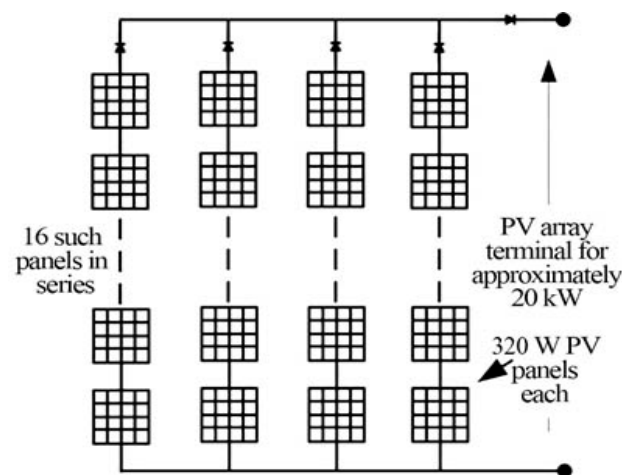

Figure 3. Mean diurnal profiles in Grenoble and Tehran. (**a**) Irradiance, (**b**) temperature.

Figure 4. Mission profile expressed in 10 different phases. Percent length of each phase in Grenoble and Tehran.

**Figure 5.** PV panel arrangement to make it an array of 20 kW.

Table 1. Grenoble and Tehran mission profile.

Phase	Grenoble				Tehran			
	h_L (Hour)	T_L (°C)	V_{pv} (V)	P_{pv} (W)	h_L (Hour)	T_L (°C)	V_{pv} (V)	P_{pv} (W)
dormant	3504	10.4	0	0	3116	16	0	0
10%	1796	11.5	610	823	1500	17	590	741
20%	975	13.4	639	3032	743	18.1	628	2974
30%	708	15.3	641	5089	637	19	634	4985
40%	468	17.1	638	7096	562	20.4	634	6997
50%	360	18.7	633	9195	501	22.2	629	8998
60%	295	19.8	629	11,270	474	24.3	624	11,001
70%	254	20.9	623	13,305	435	26.6	612	13,004
80%	223	21.7	618	15,351	410	28.4	604	14,994
90%	137	22	613	17,328	318	29.5	597	16,970
100%	40	22.1	611	19,017	65	30.1	594	18,478

Pmax = 20.533 kW

By combining the mission profile data with the efficiency curve of the inverter, the total amount of energy is obtained as Equation (2) for a duration of 25 years as follows (this duration is considered a useful lifetime of a solar panel, and industrial inverters are guaranteed by manufacturers to work without any problem in this time duration).

$$E(\text{MWh}) = 25 \text{ yr} * \sum_{i=1}^{10} P_{PVi}(\text{W}).\eta_i.t_i(\text{h}).10^{-6} \qquad (2)$$

Referring to the price of each inverter, the authors of [13] lead to the LCOE of each inverter, in EUR/MWh (Figure 6). From this figure, it is clear that the efficiency difference (Figure 2), which is due to different technological and design choices, clearly impacts the LCOE. Regardless of the inverter lifetime, which will be addressed in Section 3 of the paper, manufacturer C's inverter seems to be best choice from an LCOE perspective.
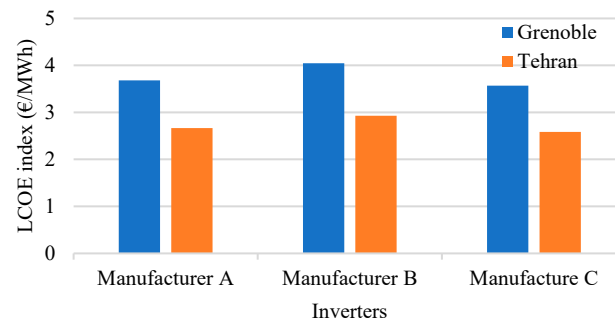

Figure 6. The LCOE index in each inverter for locations Grenoble and Tehran.

Another study case consists in choosing various sizing powers from the same manufacturer (manufacturer C's inverters in this case). By applying the mission profile to each of them, the efficiency curves (Figure 7) and finally the LCOEs are obtained. The usual PV panel degradation [14] has not been considered here for simplicity. Results, shown in Figure 8a for Tehran, show that a 17 kW sizing is the best. The same approach for Grenoble shows that a 12 kW choice would be better, according to the LCOE index applied to the inverter (Figure 8b). It is notable that there is a PV array of oversized inverters with nominal power less than 20 kW which causes some PV energy produced by panels to be lost, and, in this condition, the inverter works in its nominal power. Even though some PV energy will have been lost, this method is used to gain more energy during low solar irradiance [4]. Thus, the LCOE index shows the best choice for the inverter in a fixed-installed PV array condition.

This simple illustration of existing PV inverters shows that both technological choice and converter design impact the LCOE, and have to be considered when installing a PV inverter in a given location.
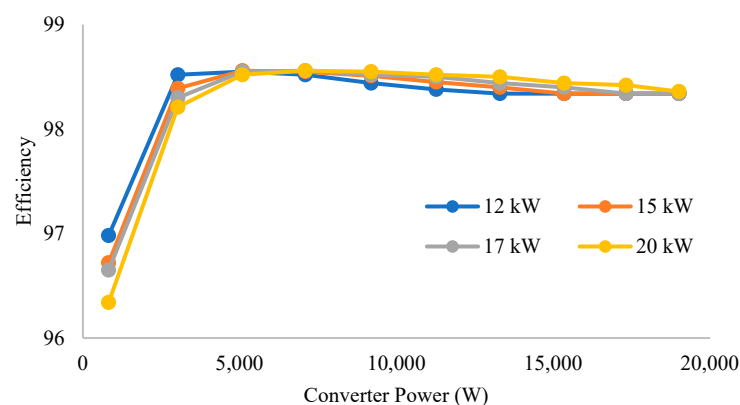

Figure 7. Efficiency curves for four different power levels.
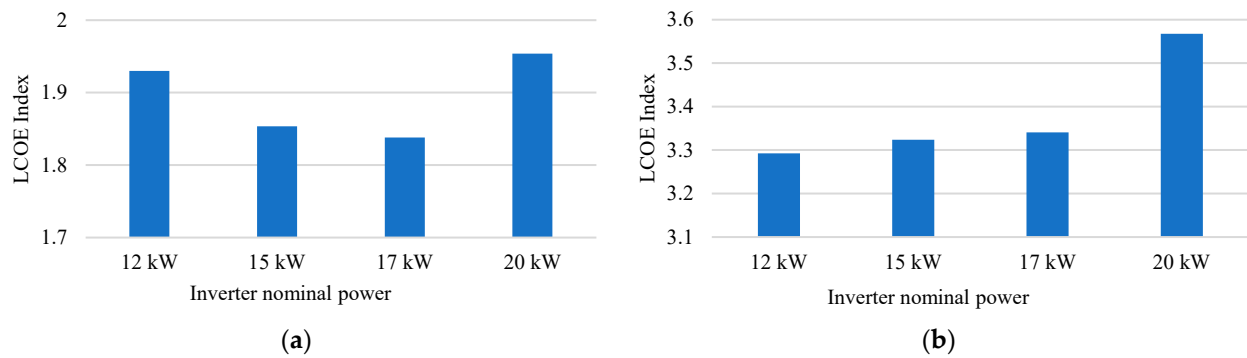
Figure 8. LCOE index for manufacturer C's inverters at location: (**a**) Grenoble (**b**) Tehran computed from values extracted from datasheet.

3. Models for Inverter Pre-Sizing

Figure 9 shows the hardware components of a PV-System from the solar array to the grid. The grid-connected photovoltaic system has two main parts: the maximum power point tracker (MPPT) and the grid-connected inverter. The MPPT is responsible for maintaining the solar array at its maximum power as well as supplying the DC link voltage in the specified value. The inverter connected to the grid is responsible for supplying the sine current injected to the grid according to the existing standards, which leads to the necessity of output filters L_1-C-L_2. Each component of the two converters (active and passive) is modeled quite accurately.
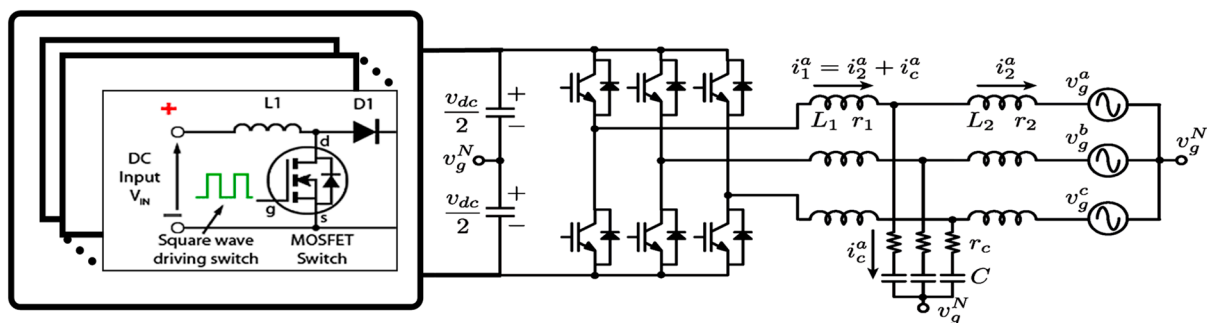
Figure 9. Different components of the grid-connected photovoltaic system.

3.1. AC Filter

In the case of PWM inverters, the design of the AC inductor is particularly critical, as it concentrates a large part of the losses of the whole system [15]. This inductor should have a significant value to decrease the ripple at the switching frequency, but should also fulfill a thermal constraint. The saturation phenomenon may decrease the inductor value during the current peak and affect the effectiveness of the filter. Therefore, it is taken into account. The design procedure of the inductor and LC filter with saturation consideration is explained in [16] and has been adapted to the LCL filter. It considers the material choice, the core, and the wiring size. The capacitors are designed according to the needed capacitance, voltage, and RMS current. To conduct this, the ripple current is assumed to be sinusoidal, at the switching frequency, and centered on the low-frequency current. These assumptions are translated into Equation (3) as follows:

$$I_{L1,AC}(t) = i_1 + i_{ripple} = \sqrt{2}I_{L1,AC}\sin(\omega t + \varphi_1) + \frac{\Delta I_{L1,AC}(t)}{2}\sin(\omega_{sw}t) \qquad (3)$$

$\Delta I_{L1,AC}(t)$ is the current ripple in the inductor at the inverter side that is variable due to the saturation effect. Thus, for simplicity, a mean ripple is defined as:

$$\Delta I_{L1,AC,mean} = \frac{1}{N_p} \sum_{i}^{N_p} \Delta I_{L1,AC}(t_i) \tag{4}$$

The ripple currents in L_2 and C are obtained by putting L_1 ripple current in filter transfer function as follows:

$$I_{L2,AC}(t) = \left| \frac{r_C + \frac{1}{j\omega_{sw}C}}{R_f + \frac{1}{j\omega_{sw}C} + j\omega_{sw}L_2} \right| \Delta I_{L1,AC}(t) \tag{5}$$

$$\Delta I_{C_f,AC}(t) = \left| \frac{j\omega_{sw}L_2}{R_f + \frac{1}{j\omega_{sw}C} + j\omega_{sw}L_2} \right| \Delta I_{L1,AC}(t) \tag{6}$$

Therefore, knowing the filter parameters, the other steps of [16] can be continued. Additionally, the THD of the injected current, which should be limited in the standard margin, is calculated by:

$$THD = 100 \frac{\frac{\Delta I_{L2,AC,mean}}{2\sqrt{2}}}{I_{L2,AC}} \tag{7}$$

3.2. Inverter Losses

A bipolar PWM pulse, computed by a comparison of a sine-wave and a triangular carrier, controls the commutation of the switches. The power losses in the inverter depend on the current and voltage patterns across the switches and on the switches sizing (i.e., voltage and current rating), which is also a design parameter. Indeed, higher current capability leads to reduced conduction losses but increased switching losses. In accordance with [17], the RMS and the average current flowing through each branch of the inverter are analytically calculated by computing switching angles. This calculation takes into account the AC current ripple, which depends on the AC output filter. Losses in the inverter are calculated by [18]. The switching frequency is also a design variable. As in [18], the losses are stated based on pure sine current, in order to consider the ripple current in calculations, the ripple current in summing in fundamental current as below:

$$i(t) = \sqrt{I_{m1}^2 + \frac{\Delta I_{L1,AC,mean}^2}{4}} \sin(\omega t + \varphi_i) \tag{8}$$

In switching losses, the switch turns on in the $i_1 - \frac{\Delta I_{L1,AC,mean}}{2}$ current and turns off in the $i_1 + \frac{\Delta I_{L1,AC,mean}}{2}$ current. Additionally, the diode turns off in the $i_1 - \frac{\Delta I_{L1,AC,mean}}{2}$ current. Therefore, energy losses in the MOSFET and diode are modified as below:

$$E_{on} = E_{on} \left(V_{dc}, i_1 - \frac{\Delta I_{L1,AC,mean}}{2} \right) \tag{9}$$

$$E_{off} = E_{off} \left(V_{dc}, i_1 + \frac{\Delta I_{L1,AC,mean}}{2} \right) \tag{10}$$

$$E_{d(off)} = E_{d(off)} \left(V_{dc}, i_1 - \frac{\Delta I_{L1,AC,mean}}{2} \right) \tag{11}$$
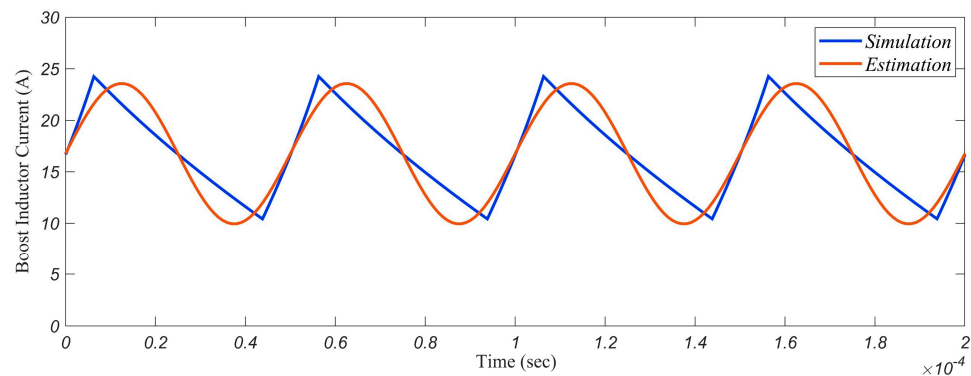
3.3. Boost Converter

The boost converter is composed of an inductor and switches. By using the same method as in previous sections of inductor design and also the switch current calculation, the output spectrum of current in the boost converter is calculated. For the purpose of

boost inductor waveform modeling, like the current in the AC filter, the ripple current is assumed to be sinusoidal at the switching frequency and superimposed on the dc part current. These assumptions are translated into Equation (12).

$$I_{Lb}(t) = I_{in} + \frac{\Delta I_{Lb}}{2}\sin(\omega_{sw,b}t) \tag{12}$$

The comparison between the modeled L_b current and the simulation result is shown in Figure 10.

Figure 10. Modeled boost converter current waveform and simulation validation.

Besides current waveforms, the losses in inductors and switches are calculated. The switching frequency is again a design variable, as well as the semiconductor sizing. In the same way, by considering the current as a ramp, the switch turns on in the $I_{in} - \frac{\Delta I_{Lb}}{2}$ current and turns off in the $I_{in} + \frac{\Delta I_{Lb}}{2}$ current. Additionally, the diode turns off in the $I_{in} - \frac{\Delta I_{Lb}}{2}$ current. Therefore, energy losses in the switch and diode are calculated as inverter losses.

3.4. DC-Link Capacitor

The DC-link capacitor is designed based on the maximum allowed ripple voltage, but also on the maximum RMS current passing through the capacitor. This current is defined in the frequency domain by $i_C = i_{boost} - i_{inv}$ of the inverter input current i_{inv} and the output current i_{boost} of the boost converter which are obtained in the previous steps. The steps for calculating the RMS current of the DC-link are explained in [17,19].

3.5. Thermal Model

Besides the dynamic and impedance modeling mentioned in [20], since the study was based on steady-state conditions, the system was modeled by thermal resistance (Rth). Junction temperature of switches and diodes are calculated based on thermal resistance from junction to ambient and limited by constraints. By supposing that all semiconductors are located on a unique heatsink, the thermal model of the case-studied photovoltaic inverter is shown in Figure 11. Each loss is evaluated from sections B and C. The thermal resistances are evaluated according to a low-power MOSFET and diode as reference semiconductors which can be paralleled by N_{sw} and N_d. In this case, the equivalent thermal resistance is calculated by dividing the reference value by the number of parallel semiconductors.

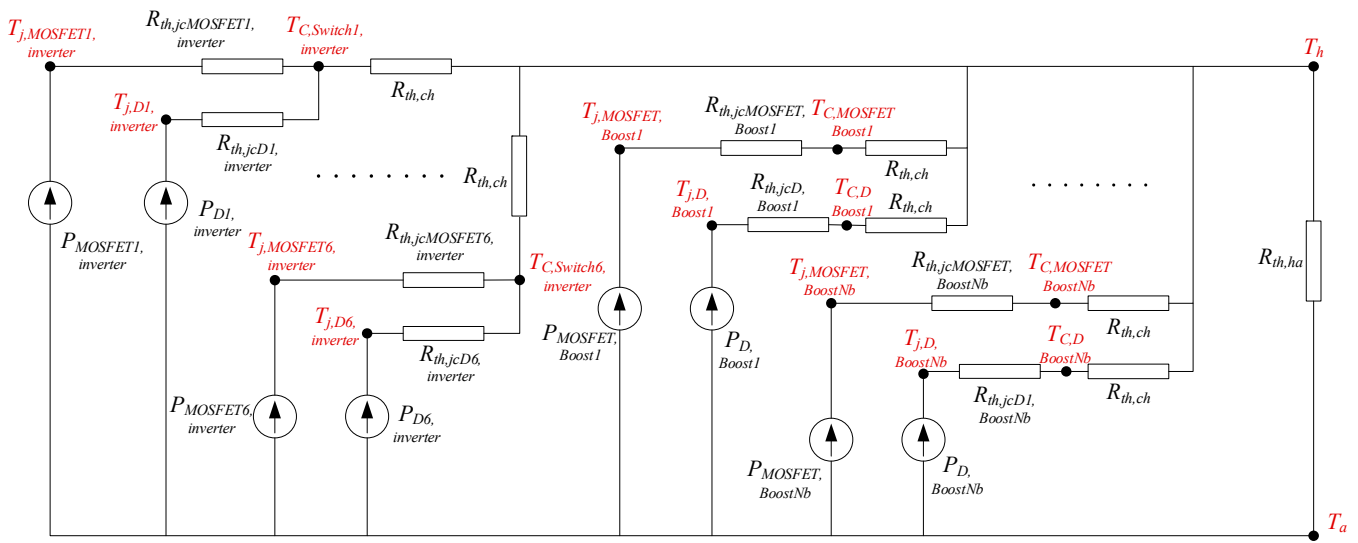$$R_{th,eq,MOSFET(diode)} = R_{th,MOSFET(diode),ref} / N_{sw(diode)} \tag{13}$$

Figure 11. Thermal model of the case-studied photovoltaic inverter.

Using the thermal model of Figure 11 allows for evaluating the temperatures of each device, being the input of reliability models. Furthermore, the maximum allowed temperature is the sizing constraint for the heatsink.

3.6. Heatsink Model

The heatsink is studied from the data of the [21] which has a large range of heatsinks in its productions. Figure 12 shows the interpolation of a large number of different heatsinks.
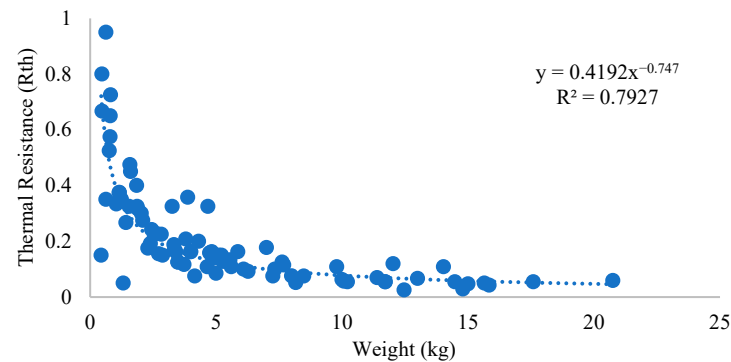

Figure 12. Thermal resistance of the heatsink according to its weight.

The thermal resistance parameter of the heatsink is expressed by its weight according to Equation (14).

$$Rth_{hs} = 0.4192W_{hs}^{-0.747} \tag{14}$$

3.7. Reliability Model

In order to obtain a longer operational lifetime, the most fragile components must be specified and reliability evaluation methodologies can be used for this approach. For this approach, the FIDES methodology is used, which is based on the physics of failure and developed by a French companies consortium. FIDES methodology is supported by the analysis of test data, field returns, and existing modeling. According to a previous evaluation, the FIDES methodology provides better results in comparison with the observed ones [12]. FIDES is a standard that defines a mathematical formula for evaluating the lifetime of devices as a function of various parameters such as operating temperature, voltage, and also manufacturing and mechanical stress [22]. Nevertheless, the most significant

parameter in reliability and lifetime evaluation is the temperature of the devices. Following the steps in [22] to evaluate the failure rate of each component in each phase of operation (λ_i^{phj}), and then each component failure rate (λ_i), the overall system failure rate is obtained by multiplying the failure rate of each component as follows:

$$\lambda_{total} = \prod_i \lambda_i \tag{15}$$

3.8. Cost Model

The individual cost of components (semiconductors, capacitors, core, and windings for inductors) have been considered, based on manufacturer prices for large ordering quantities according to the initial statement in the introduction, the total cost of the inverter has been adjusted to include a constant cost based on Figure 1 for different locations (France and Iran). Of course, this is not a perfect evaluation of the actual cost of a PV inverter, but it is sufficient for comparison purposes. In addition to the analysis of the cost of components in the markets, it can be considered by the models that are proposed in [23].

3.8.1. Semiconductor

The cost of semiconductors is defined as a function of the die area whose costs approximately scale linearly [23]. Thus, for cost evaluation, a low-power semiconductor is considered as a base and then, with the paralleling of switches, the amount of cost is calculated simply.

$$C_{sc} = N_{sc}C_{sc,ref} \tag{16}$$

3.8.2. Capacitors

The main types of power capacitors in the field of power electronics are electrolytic and film capacitors. The capacitors are investigated using data sheets from different manufacturers [24,25]. Data are collected and then compared. It is deduced that most of the design parameters of capacitors, such as cost, ESR, etc., depend on the capacitance (C) and voltage rating (V). Figure 13 shows the estimated model for the cost of FILM capacitors.
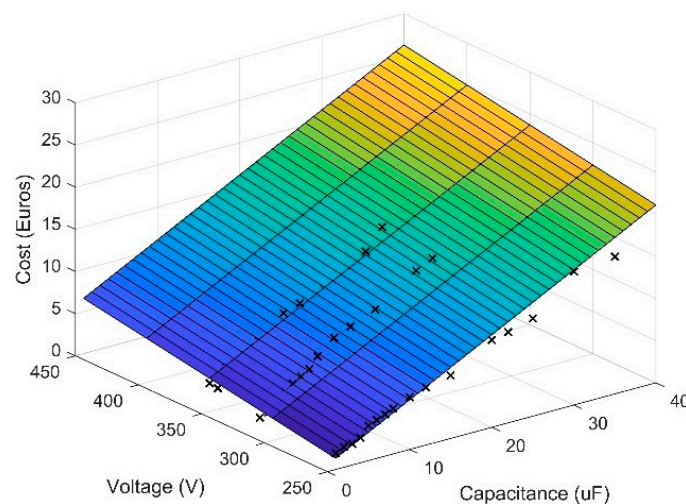
Figure 13. Estimation of the cost of a film capacitor.

The data reveal the price dependencies of the considered film capacitors, scaled linearly with the rated capacitance C and voltage rating V, whereas the electrolytic capacitor is linked to stored energy ($\propto CV^2$) [23]. Based on this, the following cost models are supposed for film and electrolytic capacitors.

$$Cost_{Cf} = -5.693 + 0.0261 * V_{Cf} + 0.5063 * C_f \tag{17}$$

$$Cost_{Cdc} = 1.437 * 10^3 * V_{Cdc} + 24.757 * 10^{-9} * V_{Cdc}^2 * C_{dc} \tag{18}$$

3.8.3. Inductors

The inductors' cost is defined based on core and wires cost as their BOM. The choice of the core is based on the iron powder core of [26]. There are several core materials and permeabilities. According to [27], the KoolMu material with a permeability of 60 is the best choice in terms of weight and cost. The core data show a linear relationship between core weight and core volume, with volume defined by core dimensions as the design variable. Considering core dimensions depicted in Figure 14, the volume of the core is calculated by Equation (19).
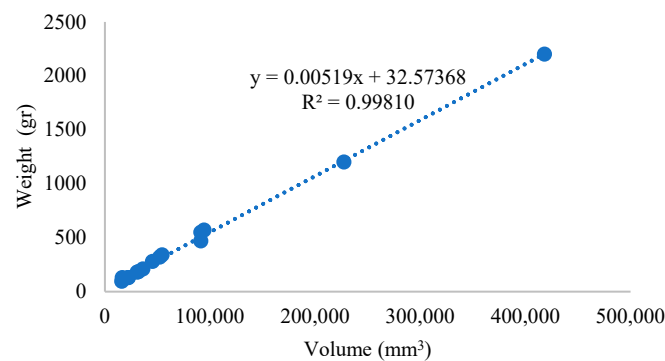
$$Vol = \pi * \left(R_{out}^2 - R_{in}^2 \right) * H \tag{19}$$
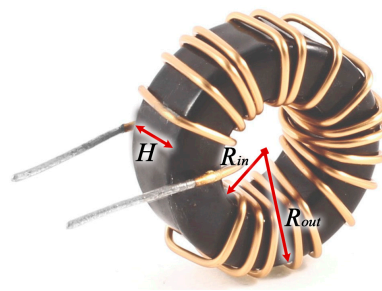
Figure 14. The toroidal core dimensions.

The linear relationship between core weight and core volume is shown in Figure 15. Considering EUR 30 per kilogram [27], the cost of the core is calculated according to its dimensions as Equation (20).
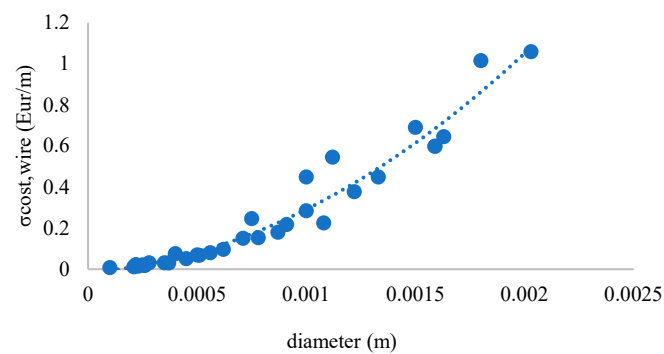
$$Cost_{Core} = 30 * (0.00519 * Vol + 32.57368) * 10^{-3} \tag{20}$$

Figure 15. The weight and volume relationship.

The winding is considered to be wound by a plain copper wire in a single layer. By gathering data from [28], the cost of wire in the length unit is calculated based on diameter. The interpolation of data is shown in Figure 16 and stated in Equation (21).

$$\sigma_{Cost,wire} \left(\frac{\text{€}}{m} \right) = 225,832.61 d_s^2 + 81.46 d_s - 0.02 \tag{21}$$

**Figure 16.** The fitting of plain copper wire cost per meter.

Finally, by the length of winding which is obtained by design variables (turn number and core dimensions), the cost of winding is calculated by Equation (22).

$$Cost_{wire} = \sigma_{Cost,wire} * lentgh_{winding} \tag{22}$$

3.8.4. Heatsink

By investigating different products of [29], it is deduced that the design parameters of the heatsink such as cost and thermal resistance are related to the weight. As shown in Figure 17, the heatsink cost has a linear relationship with weight and is expressed as Equation (23).

$$Cost_{hs} = 13.85W_{hs} + 16.494 \tag{23}$$
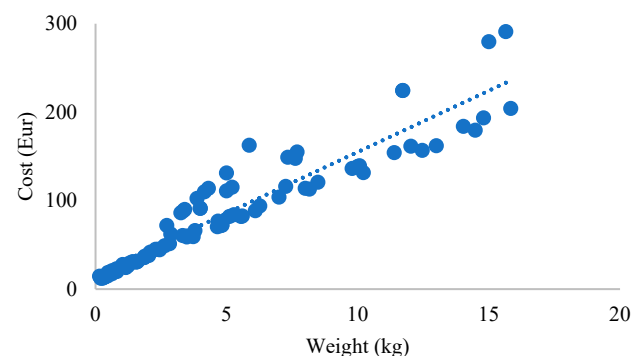
Figure 17. The fitting of the heatsink cost.

4. LCOE Estimation for Various Case Studies

All previous models have been developed, taking care of derivability in order to be used with a deterministic algorithm (sequential quadratic programming method (SQP) [30]). This presents the advantage of being very effective in quickly finding the optimum in a large space of solution, with large amounts of variables and constraints. The model indeed is composed of more than 25 parameters and 50 constraints (at the component or system level). The design framework used is able to perform automatically the derivation of all equations, leading to significant time-saving. The objective function is to reach the minimum cost for a given sizing power. In the optimization process, the reliability is forced to be at least more than 25 years to be insured that the inverter could work in the PV panels' lifetime. For each optimized inverter, the mission profile is applied. Of course, the maximum power is limited to the sizing power during operation. It is noticed that overload capability has not been considered since the models cannot handle the consequence of this kind of overload. Consequently, the converter is exactly sized regarding nominal power, without any margin. Figure 18 shows the design level of the optimization procedure where the design variables in each iteration are chosen. More than 25 variables are considered

including filter parameters (core size and turn number for inductors), switching frequencies (inverter and boost converters), number of switches, etc. The set of design variables should satisfy some constraints on THD, the junction temperature of switches, diodes, and rise temperature in capacitors. Then, the LCOE index is evaluated by combining the results of Sections 3.7 and 3.8 and the best set of design variables chosen. The flowchart of LCOE optimization is presented in Figure 19.
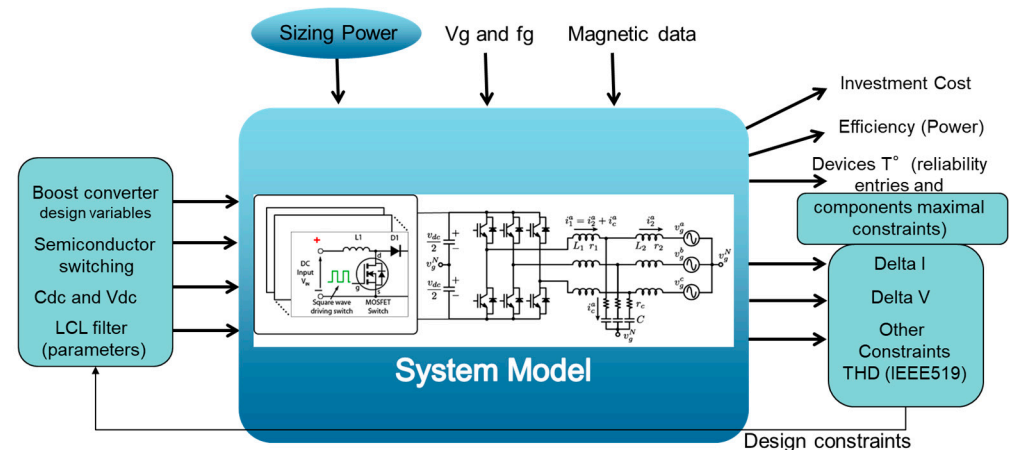

Figure 18. The design level of optimization procedure considering design variables as input.
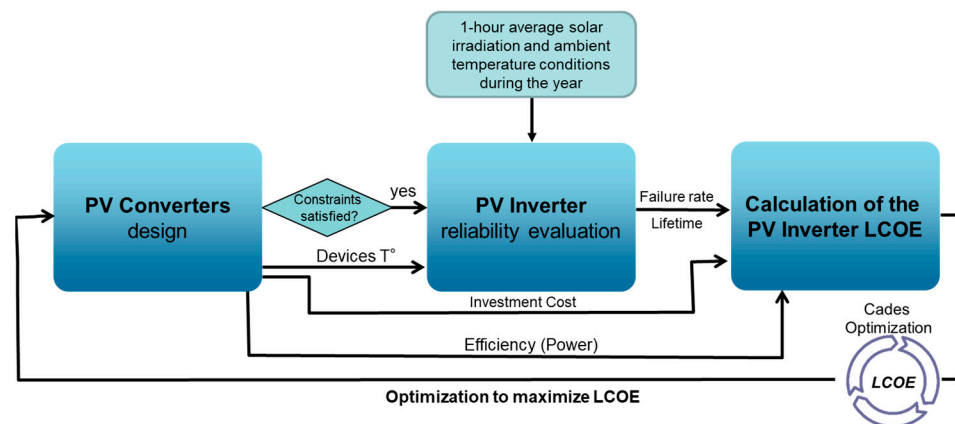

Figure 19. The flowchart of LCOE optimization.

Results of LCOE for Grenoble and Tehran are displayed in Figure 20. It is worth noting that the optimal sizing power is different for the two locations according to the different solar irradiation. This confirms the results from previous work, which showed the interest in downsizing the nominal power to gain more energy yield during low solar irradiance conditions [4]. Note that the LCOE index is applied to the inverter only and that the inverter cost is reduced to the sum of components cost, therefore absolute values of sizing power are not to be considered as a strict result, but only for comparison purposes (see conclusion).

Another interest of the approach is that it allows for investigating the impact of some technological choices. For instance, using SiC-MOSFET or Si-IGBT has been illustrated in Figure 21 for the location Tehran. It is worth noting that IGBT, despite its lower cost, leads to higher LCOE. Indeed, its higher switching losses lead to reduced switching frequency (16 kHz roughly for each design, which was the minimum imposed for the audition limit), leading to higher costs for passive components, specifically to meet the THD constraint.
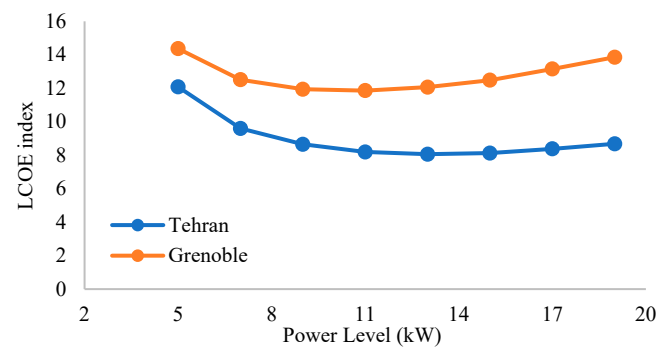
Figure 20. LCOE index comparison for Grenoble and Tehran.
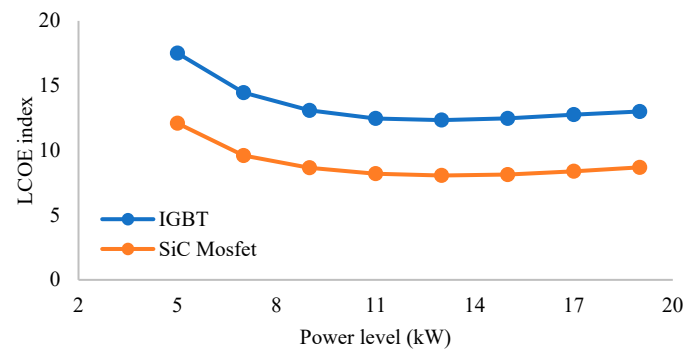
Figure 21. LCOE index Si vs. SiC (Tehran).

Another technological choice that can be considered is the comparison of the wire material between copper and aluminum. The LCOE index for both materials is presented in Figure 22, where this index is almost the same for both cases, whereas aluminum is cheaper than copper in the markets but the resistivity coefficient of aluminum (ρ) is higher than that of copper [31], causing more power losses in the system. Thus, the injected energy is lower than in the other case. It should be noted that the temperature coefficient (α) is not considered in this study, and since this coefficient is higher in aluminum than in copper, the LCOE can be expected to be higher than the one presented.
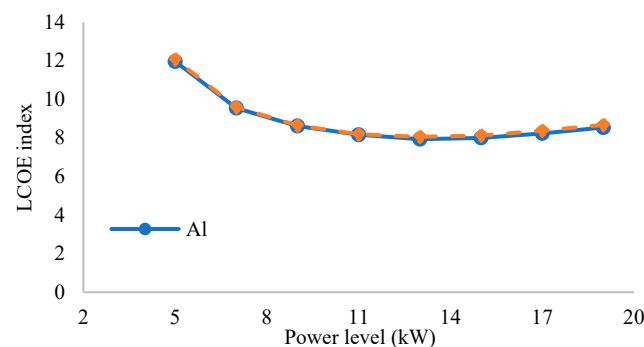
Figure 22. LCOE index copper vs. aluminum (Tehran).

As mentioned in Section 3, cost models are very difficult to establish and the considered cost models are based on component costs. Another possibility is to use the expertise of engineers. A database from SIREPE was used for this purpose. The data can be expressed and considered in the design process as proportional to component cost with a gain ($C_{model\#1} = k_1 C_{BoM}$) or by adding a constant value ($C_{model\#2} = k_2 C_{BoM} + k_3$). These two visions are considered and compared with base results which are obtained before by the cost of components. As shown in Figure 23, the new indexes are higher than the base ones due to the increment in cost, but the optimal point is not affected by the cost model.
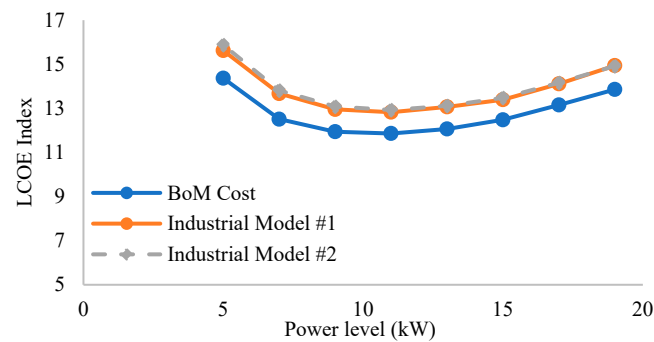
Figure 23. LCOE index for different cost models (Grenoble).

5. Conclusions

Considering the actual sizing and technological choice for PV inverters determines how to solve the tradeoff between inverter cost and its performance during its lifetime. This paper first illustrates the impact of these parameters on existing inverters by using the LCOE index (applied to power electronics only). Then, an optimization method is proposed, using detailed models of components, in order to obtain the best sizing power for the inverter, according to the LCOE index and a given mission profile. The design method accounts for components and system-level constraints. It is also applied to investigate the impact of semiconductors and material choice. Additionally, a sensitivity analysis of the cost model is performed.

Author Contributions: Conceptualization, M.T.-N. and S.F.; methodology, M.T.-N. and J.-L.S.; software, M.T.-N.; validation, M.T.-N. and J.-L.S.; formal analysis, M.T.-N. and C.R.; investigation, M.T.-N.; resources, M.T.-N. and C.R.; data curation, M.T.-N. and C.R.; writing—original draft preparation, M.T.-N.; writing—review and editing, J.-L.S. and H.I.-E.; visualization, M.T.-N.; supervision, J.-L.S., S.F. and H.I.-E.; project administration, S.F. and J.-L.S.; funding acquisition, S.F. and J.-L.S. All authors have read and agreed to the published version of the manuscript.

Conflicts of Interest: The authors declare no conflict of interest.

References

1. Feldman, D.; Ramasamy, V.; Fu, R.; Ramdas, A.; Desai, J.; Margolis, R.U.S. *Solar Photovoltaic System Cost Benchmark: Q1 2020*; NREL/TP-6A20-77324; National Renewable Energy Laboratory: Golden, CO, USA, 2021.
2. Keller, L.; Affolter, P. Optimizing the panel area of a photovoltaic system in relation to the static inverter—Practical results. *Sol. Energy* **1995**, *55*, 1–7. [CrossRef]
3. Koutroulis, E.; Blaabjerg, F. Design Optimization of Transformerless Grid-Connected PV Inverters Including Reliability. *IEEE Trans. Power Electron.* **2012**, *28*, 325–335. [CrossRef]
4. Sangwongwanich, A.; Yang, Y.; Sera, D.; Blaabjerg, F. Mission Profile-Oriented Control for Reliability and Lifetime of Photovoltaic Inverters. In Proceedings of the 2018 International Power Electronics Conference (IPEC-Niigata 2018-ECCE Asia), Niigata, Japan, 20–24 May 2018; pp. 2512–2518. [CrossRef]
5. Kadri, R.; Gaubert, J.-P.; Champenois, G. An Improved Maximum Power Point Tracking for Photovoltaic Grid-Connected Inverter Based on Voltage-Oriented Control. *IEEE Trans. Ind. Electron.* **2010**, *58*, 66–75. [CrossRef]
6. Nasiri, R.; Khayamy, M.; Rashidi, M.; Nasiri, A.; Bhavaraju, V. Optimal Solar PV Sizing for Inverters Based on Specific Local Climate. In Proceedings of the 2018 IEEE Energy Conversion Congress and Exposition (ECCE), Portland, OR, USA, 23–27 September 2018; pp. 6214–6219. [CrossRef]
7. Velasco, G.; Guinjoan, F.; Pique, R.; Conesa, A.; Negroni, J. Inverter power sizing considerations in grid-connected PV systems. In Proceedings of the 2007 European Conference on Power Electronics and Applications, Aalborg, Denmark, 2–5 September 2007; pp. 1–10. [CrossRef]
8. Kratzenberg, M.G.; Deschamps, E.M.; Nascimento, L.; Rüther, R.; Zürn, H.H. Optimal Photovoltaic Inverter Sizing Considering Different Climate Conditions and Energy Prices. *Energy Proc.* **2014**, *57*, 226–234. [CrossRef]
9. Solar, S.M.A.; Ag, T. INTEGRATED Service for Ease and Comfort. Available online: https://files.sma.de/downloads/STP15-25TL-30-DS-en-41.pdf (accessed on 23 April 2021).

10. Fronius. Fronius Symo Datasheet. Available online: http://www.fronius.com/ (accessed on 22 September 2020).
11. Huawei. Smart String Inverter. SUN2000-12/15/17/20KTL-M0 Datasheet, 2019. Available online: https://solar.huawei.com/-/media/Solar/attachment/pdf/apac/datasheet/SUN2000-12-20KTL-M0.pdf (accessed on 22 October 2020).
12. De Leon-Aldaco, S.E.; Calleja, H.; Alquicira, J.A. Reliability and Mission Profiles of Photovoltaic Systems: A FIDES Approach. *IEEE Trans. Power Electron.* **2014**, *30*, 2578–2586. [CrossRef]
13. Solar inverters. Solar Inverter for PV System | Europe Solar Store. Available online: https://www.europe-solarstore.com/solar-inverters.html?inverter_power=24 (accessed on 22 October 2020).
14. Sangwongwanich, A.; Yang, Y.; Sera, D.; Blaabjerg, F. Lifetime Evaluation of Grid-Connected PV Inverters Considering Panel Degradation Rates and Installation Sites. *IEEE Trans. Power Electron.* **2017**, *33*, 1225–1236. [CrossRef]
15. Orłowska-Kowalska, T.; Blaabjerg, F.; Rodríguez, J. *Advanced and Intelligent Control in Power Electronics and Drives*; Springer: Cham, Switzerland, 2014; Volume 531.
16. Voldoire, A.; Schanen, J.; Ferrieux, J.; Gautier, C.; Saber, C. Optimal Design of an AC Filtering Inductor for a 3-Phase PWM Inverter Including Saturation Effect. In Proceedings of the 2019 10th International Power Electronics, Drive Systems and Technologies Conference (PEDSTC), Shiraz, Iran, 12–14 February 2019; pp. 595–599. [CrossRef]
17. Voldoire, A.; Schanen, J.-L.; Ferrieux, J.-P.; Gautier, C.; Saber, C. Analytical Calculation of DC-Link Current for N-Interleaved 3-Phase PWM Inverters Considering AC Current Ripple. In Proceedings of the 2019 21st European Conference on Power Electronics and Applications, Genova, Italy, 3–5 September 2019. [CrossRef]
18. Ahmed, M.H.; Wang, M.; Hassan, M.A.S.; Ullah, I. Power Loss Model and Efficiency Analysis of Three-Phase Inverter Based on SiC MOSFETs for PV Applications. *IEEE Access* **2019**, *7*, 75768–75781. [CrossRef]
19. Kolar, J.; Round, S. Analytical calculation of the RMS current stress on the DC-link capacitor of voltage-PWM converter systems. *IEE Proc.-Electr. Power Appl.* **2006**, *153*, 535–543. [CrossRef]
20. Shen, Y.; Song, S.; Wang, H.; Blaabjerg, F. Cost-Volume-Reliability Pareto Optimization of a Photovoltaic Microinverter. In Proceedings of the 2019 IEEE Applied Power Electronics Conference and Exposition (APEC), Anaheim, CA, USA, 17–21 March 2019; pp. 139–146. [CrossRef]
21. Wakefield Thermal Air Cooled Thermal Extrusions. Available online: https://wakefieldthermal.com/thermal-solutions/air-cooled/thermal-extrusions/ (accessed on 26 February 2019).
22. FIDES Guide 2009. Edition A. Reliability Methodology for Electronic Systems. 2010. Available online: www.fides-reliability.org (accessed on 29 September 2010).
23. Burkart, R.; Kolar, J.W. Component cost models for multi-objective optimizations of switched-mode power converters. In Proceedings of the 2013 IEEE Energy Conversion Congress and Exposition, Denver, CO, USA, 15–19 September 2013; pp. 2139–2146. [CrossRef]
24. Capacitors Datasheet, Vishay. Available online: https://www.vishay.com/en/capacitors/ (accessed on 15 June 2020).
25. Capacitors Datasheet, TDK. Available online: https://product.tdk.com/en/products/capacitor/index.html (accessed on 10 September 2019).
26. Powder Cores Datasheets, Magnetics. Available online: https://www.mag-inc.com/Products/Powder-Cores (accessed on 17 August 2017).
27. Voldoire, A. Outil de Développement et D'optimisation Dédié aux Onduleurs SiC de Forte Puissance. Doctoral Dissertation, Université Grenoble Alpes, Saint-Martin-d'Hères, France, 2020.
28. Energy Chains, Polymer Bearings, Flexible Cable & Linear Slides. Available online: https://www.igus.co.uk/ (accessed on 15 June 2020).
29. Wakefield-Vette Heat Sinks–Mouser Europe. Available online: https://eu.mouser.com/c/thermal-management/heat-sinks/?m=Wakefield-Vette (accessed on 15 June 2020).
30. Boggs, P.T.; Tolle, J.W. Sequential Quadratic Programming. *Acta Numer.* **1995**, *4*, 1–51. [CrossRef]
31. Giancoli, D.C. *Physics*, 4th ed.; Prentice Hall: Hoboken, NJ, USA, 1995.